JASA ARTICLE

Bioinspired flow-sensing capacitive microphone

Johar Pourghader,[1,a)] Weili Cui,[2] Mahdi Farahikia,[3] Junpeng Lai,[1] Morteza Karimi,[1] Changhong Ke,[1] and Ronald Miles[1,b)]

[1]*Department of Mechanical Engineering, Binghamton University, Binghamton, New York 13902, USA*

[2]*Department of Mechanical and Facility Engineering, State University of New York, Maritime College, Bronx, New York 10465, USA*

[3]*Division of Engineering Programs, State University of New York at New Paltz, New Paltz, New York 12561, USA*

ABSTRACT:

Inspired by the auditory systems of small animals, such as spiders, the tachinid fly, *Ormia ochracea*, and mosquitoes, a novel low-noise, flow-sensing capacitive MEMS microphone capable of sensing acoustic particle velocity is introduced. Unlike conventional microphones that have a diaphragm for sensing sound pressure, this design consists of a thin, porous, movable structure that is intended to be driven by viscous forces as a result of the sound-induced flow. This viscous force then rotates the movable structure around a middle central hinge and creates a change in capacitance caused by a relative motion between neighboring beams. The whole structure is made of one layer of silicon using a silicon-on-insulator (SOI) wafer using photolithography technology with a device layer thickness of 5 μm. The movable part has dimensions of 0.7 mm $\times$ 1.2 mm and is placed above a cavity inside the bulk silicon that facilitates the flow of sound particles. This microphone responds to flow (a vector) rather than pressure (a scalar). Ultimately, experimental results demonstrate a sensitivity of approximately 5 mV/Pa, a noise floor between 10^{-4} and 10^{-5} Pa/$\sqrt{\text{Hz}}$, and directivity ratios reaching up to 77 at 2000 Hz, underscoring its potential for high-performance acoustic applications. https://doi.org/10.1121/10.0036772

(Received 26 December 2024; revised 10 April 2025; accepted 5 May 2025; published online 23 May 2025)

[Editor: Thomas Edward Blanford] Pages: 3897–3906

I. INTRODUCTION

Much can be learned about the design of microphones by studying the physical principles used by animals for sensing sound. The main purpose of this paper is to explore the design of a microphone based on principles that have proven effective in natural designs but have received scant attention in engineered designs. The primary result presented in the following is a prototype microphone design that employs principles that, as far as we are aware, have not been used in previous man-made designs. Because most animals detect sound by sensing the airflow that occurs in a sound field rather than sound pressure, the device examined here is designed to detect acoustic flow; this is a departure from the usual practice.

Small animals that are able to hear, such as insects, typically detect sound by employing sensory hairs or antennae, which are driven by viscous forces from the surrounding sound-induced fluid motion (Barth *et al.*, 1993; Coombs, 2001; Landolfa and Jacobs, 1995; Shimozawa *et al.*, 1998; Tautz, 1979; Tautz and Markl, 1978). Man-made hair-like structures, such as micro-scale silicon beams, which also respond to viscous forces, can be fabricated. We have shown that the dependence of the acoustic performance on key design parameters of viscous flow-driven structures such as these can be different from what designers are familiar with in classical pressure-sensing microphone designs (Lai *et al.*, 2024). Because viscous flow-driven structures have potential for teaching us about sensing sound, they warrant attention by microphone designers; designers have almost no experience in creating them. Our previous investigations of viscous-driven acoustic sensors suggest there could be significant advantages regarding the required size and achievable thermal noise floor of these sensors (Lai *et al.*, 2024). The primary focus of the present effort is to consider one possible approach at creating a design that is compatible with current silicon microfabrication processes.

Various endeavors have been made to develop acoustic particle velocity sensors, with many of them drawing inspiration from the auditory mechanisms observed in small animals (Humphrey and Barth, 2007; Humphrey *et al.*, 1993; McHenry *et al.*, 2008; McHenry and van Netten, 2007). To show the viability of the concept of acoustic flow sensing inspired by the cerci of crickets' sensory hairs, an array of beams oriented perpendicularly to a plane surface and made of SU-8 was used along with a capacitive readout for frequencies less than 100 Hz (Chen *et al.*, 2003; Dijkstra *et al.*, 2005; Fan *et al.*, 2002; Krijnen *et al.*, 2006). Inspired by hair cells in nature, artificial hairs have also been integrated with piezoresistive materials to obtain an electronic output. In these flow sensors, the movement of the hair-like structure causes deformation-induced changes of resistance that can be measured with a Wheatstone bridge (Han *et al.*, 2018; Moshizi *et al.*, 2020).

[a)]Email: jpourgh1@binghamton.edu
[b)]Email: miles@binghamton.edu

The ribbon microphone is often referred to as a "velocity" microphone. The ribbon is designed, however, to respond to the difference in pressure on each of its planar surfaces rather than to respond to viscous forces in the acoustic flow (Weinberger *et al.*, 1933). The ribbon is, thus, driven by the same force that causes the air to move; for a sufficiently lightweight and compliant ribbon, its motion will be a reasonably close approximation to that of the air. The driving force is, therefore, essentially the same as that of any pressure-sensing diaphragm in which its two surfaces are exposed to the sound field. The intent of the present design, however, is to rely on viscous forces in the moving air to drive the sensing structure rather than sensing pressure, as is performed in essentially all microphones.

Flow sensors based on the flow-induced dissipation of heat in a thin wire have been commercialized and well-studied for years (Chen *et al.*, 2003). An array based on MEMS hot-wire anemometry was used for underwater application (Chen *et al.*, 2006; Pandya *et al.*, 2006; Yang *et al.*, 2006; Yang *et al.*, 2010). The μ-flown is a commercially available instrument that uses two thin platinum wires as temperature sensors to detect the acoustic flow based on the change in electrical resistance as a result of temperature changes in the electrodes caused by acoustic particle velocity (De Bree, 2003; Farkasosvká and Bil'ová, 2012; Van Der Eerden *et al.*, 1998).

To incorporate these viscous flow-sensing structures in a typical silicon microfabrication process, the sensing structures are oriented orthogonally to the chip substrate. As a result, the fabrication of the sensors examined in Chen *et al.* (2003), Dijkstra *et al.* (2005), Fan *et al.* (2002), and Krijnen *et al.* (2006) requires methods that deviate substantially from standard silicon microfabrication processes that are used to create the billions of pressure-sensing silicon microphones currently produced.

A typical fabrication process for silicon microphones involves creating a sacrificial insulation layer (such as silicon oxide) on a wafer, depositing a material to create a pressure-sensing diaphragm (such as polycrystalline silicon), and performing a through-wafer etch from the backside to create an air space underneath the pressure-sensing diaphragm (Dagher, 2020; Ozdogan *et al.*, 2020; Peng *et al.*, 2025). Although the details vary, these microphones generally require a sensing film or diaphragm which is backed by an air-filled cavity. The diaphragm is, therefore, oriented parallel to the top surface of the silicon wafer. The fabrication of the flow-sensing microphone examined here consists of similar steps to those of conventional silicon microphones. The silicon flow-sensing structure is also fabricated over an air-filled cavity using a similar process. A schematic of the present system consisting of fixed and movable capacitive electrodes is displayed in Fig. 1.

The moving structure of Fig. 1 embodies a combination of principles for detecting sound that has been demonstrated in nature. One principle is to employ the viscosity of air to drive thin structures as the air moves in a sound field. We have described one inspiration for this in an examination of hearing by an orb-weaving spider, which detects sound through the acoustic flow-driven vibration of its web (Zhou *et al.*, 2022).

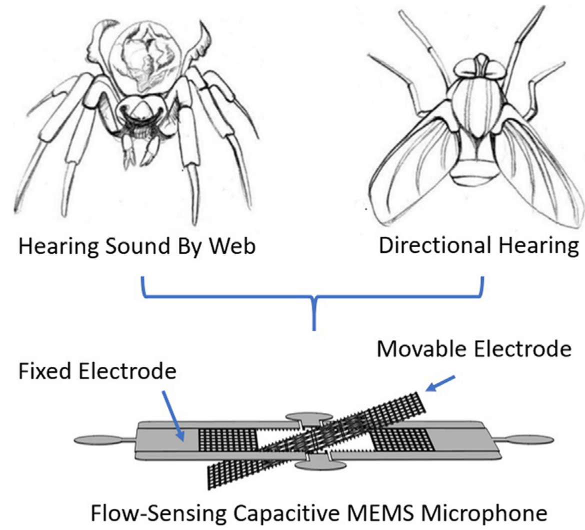

FIG. 1. Schematic of the device layer for the bioinspired capacitive MEMS microphone. The design integrates flow-sensing mechanisms inspired by the spider's auditory system (spider web) and the rocking motion of a rotatable movable electrode, modeled after the hearing system of the *Ormia ochracea* fly. This combination enables capacitive sensing by using the flow of acoustic particles and attenuates sound from unwanted directions.

Rather than require a flow-sensing structure that protrudes orthogonally from the silicon substrate, it can be beneficial to incorporate some sort of cavity beneath the sensing structure that can redirect the acoustic particle velocity such that it flows into and out of the cavity. The flow direction will then be normal to the planar surface of a silicon chip (Lai *et al.*, 2025). This cavity would be created using the same through-wafer etch as is used to create the air space behind a pressure-sensing diaphragm. The flow-sensing structure, although not a pressure-sensing diaphragm, could be fabricated by depositing material on the top of the wafer, using a process identical to that of the sensing material employed to create a pressure-sensing diaphragm. The use of the cavity to redirect the flow to drive the moving element in the direction normal to the substrate has been inspired by our earlier investigation of the hearing of the parasitoid fly *Ormia ochracea* (Miles *et al.*, 1995; Miles *et al.*, 2009). The spider and fly that inspired this work are depicted in Fig. 1.

The sensing structure transduces the sound-induced motion into an electronic signal through capacitive sensing. The result is a candidate design for a capacitive flow-sensing microphone that is produced using essentially the same fabrication process that is required for conventional MEMS microphones.

Sensing acoustic particle velocity holds significant utility in acoustic studies. Knowing acoustic particle velocity and pressure permits a comprehensive characterization of acoustic phenomena (Miles, 2020). Viscous flow-driven velocity-sensing microphones offer a direct means of capturing acoustic particle velocity, a capability previously achieved using a minimum of two pressure-sensing microphones.

https://doi.org/10.1121/10.0036772

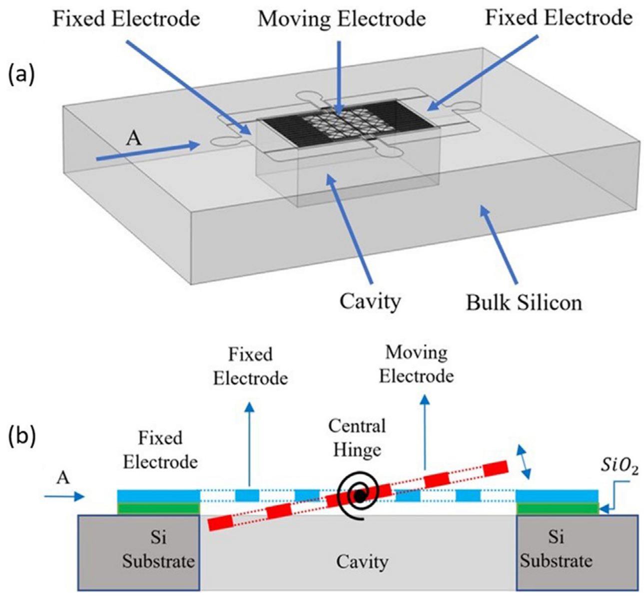

FIG. 2. Schematic of interdigitated fingers of the fixed and moving electrodes on the cavity. (a) 3D view and (b) a simplified 2D cross-sectional view show an exaggerated deflection of the movable electrode. When sound propagates in the direction (A), the microphone achieves its maximum sensitivity. This direction is perpendicular to the axis of rotation (i.e., the hinge) and in the plane of the sensing structure.

The application of a velocity-sensing pair, as used for acoustic intensity measurements, requires increased inter-microphone spacing at lower frequencies, thereby presenting a challenge for miniaturization (Miles, 2020). By measuring acoustic particle velocity, frequency-independent directivity is achieved, rendering this technology well-suited for applications in which the size of the array is to be minimized and when localizing sound sources in the presence of background noise and reflections (Zhang *et al.*, 2019).

The acoustic flow-sensing device examined here, as shown schematically in Fig. 1, consists of two fixed electrodes and a moving electrode to enable capacitive sensing. The moving structure is placed above the air-filled cavity such that acoustic flow into and out of the cavity causes the moving electrode to rotate about a central hinge. As mentioned above, we have conducted a detailed examination of the design of such a cavity so that it essentially redirects the sound-induced flow from the direction parallel to the surface of the chip to be into and out of the cavity. This enables the use of a sensing structure placed at the top or opening of the cavity. It is shown that the device is able to detect sound over a substantial portion of the audible frequency range. The sound-induced velocity of the moving electrode is very similar to the acoustic particle velocity in a plane wave sound field. A schematic of the moving and fixed electrodes over the cavity is displayed in Fig. 2.

In the following, we describe the main components of the sensor, including the flow-sensing electrodes and capacitive transduction to obtain an electronic signal. Then, measured results are presented that show that this concept leads to a working flow-sensing microphone, which is fabricated using conventional microfabrication methods.

A. Fabrication process

The structure shown in Figs. 3 and 4 has been fabricated using a silicon-on-insulator (SOI) wafer consisting of a 500 μm thick bulk silicon wafer having a 1 μm layer of SiO_2 with a 5 μm thick single crystal silicon doped device layer. The device layer was patterned using a single photolithographic mask and etched to construct the structure. A back-side etch was then performed to create a through-wafer cavity in the bulk silicon wafer behind the moving structure. The structure was then released by etching the 1 μm layer of SiO_2.

B. Movable electrode

The moving electrode depicted in Fig. 4 is formed by patterning the 5 μm thick device layer of a SOI wafer, followed by a back-side etch of the bulk silicon to create a back-side cavity. The movable structure is supported by a flexible central hinge, which is shown in Figs. 3(a) and 3(b), that enables the rotation of the whole structure around its central axis. As the pattern is created using photolithography using a single mask and a single etch, the thickness is the

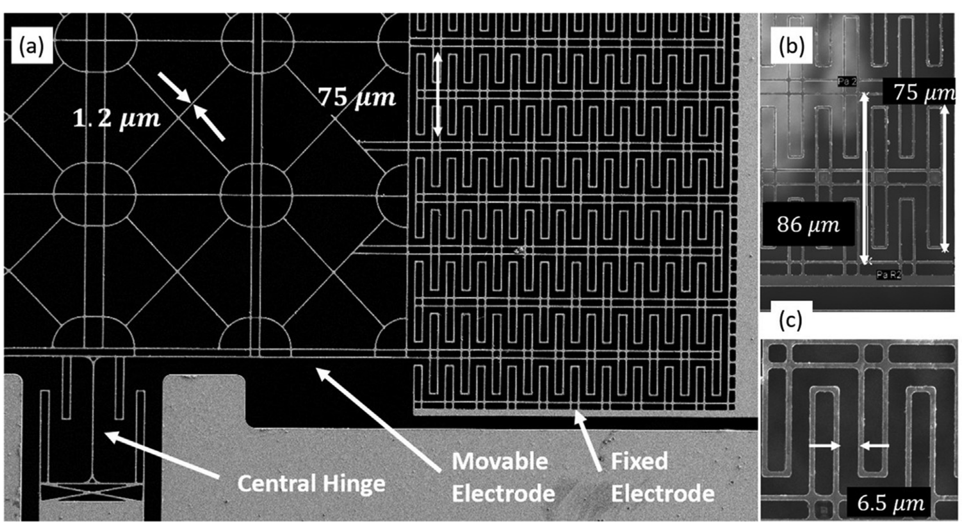

FIG. 3. SEM image of the interdigitated fingers. (a) A quarter of the movable electrode with its neighboring fixed fingers is displayed; (b) and (c) show a close-up of the combs. The finger width is 1.2 μm for the fixed and moving electrodes, and the gap between the electrodes is 6.5 μm.

same throughout the device layer. The width of all the thin beams, including fingers and hinges, is 1.2 μm. The thickness of the device layer and, hence, the moving electrode is 5 μm. This makes the hinge cross section rectangular with dimensions of 5 μm $\times$ 1.2 μm with a length of 100 μm. The equivalent torsional stiffness is approximately $K_t = 3.8 \times 10^{-9}$ N m/rad with a mass of $m = 5.6 \times 10^{-10}$ kg and a mass moment of inertia around the hinge of $I_m = 6.9 \times 10^{-17}$ kg m^2. This results in a natural frequency of 1179 Hz, without the influence of electrostatic forces, which is 13% higher than the experimentally measured natural frequency of 1037 Hz. Applying a bias voltage of 6 V increases the natural frequency to 2500 Hz.

A response that is reasonably independent of frequency over the audible frequency range is desired. To achieve this, there should be as few resonant modes in the audible range as possible. An effort has been made to have only one resonant mode with a frequency as low as feasible. An effective design can be achieved by using a structure that has low mass, high moment of inertia, and is supported on flexible torsional hinges. The structure should also have high bending stiffness such that it behaves as a rigid body.

To decrease the first natural frequency and also make use of the higher displacements at the ends of the moving structure, the fins that allow capacitive sensing are placed in the portion of the structure furthest from the center of rotation. This helps to maximize the capacitive change caused by the rotation of the moving electrode. In addition, to ensure that the structure is moved by the acoustic particle velocity rather than sound pressure, the width of the fins is designed to be less than 5 *μm* to maximize the viscous drag force (Miles *et al.*, 2019).

C. Fixed electrodes

Fixed electrodes, consisting of interdigitated fins similar in shape to the moving fins, are placed at each end of the moving element. The thickness of the fixed electrodes is equal to that of the 5 μm thick device layer of the SOI wafer, which is placed over 1 μm of the insulating layer (SiO_2) above 500 μm of bulk silicon. Decreasing the size of the gap between the fixed and moving parts will increase the total capacitance. Unfortunately, it will also increase the shear viscous forces between fixed and moving parts, adding viscous damping, which will adversely affect the structure's response to sound. This gap is designed to be set as 6.5 μm. This is, again, a design parameter that could be optimized in a future study. An initial investigation of the design of these fins is presented in Fig. 9.10 of Miles (2020).

D. Flow-sensing mechanism

The viscous force is the dominant force resulting from sound in thin microbeams having a width of less than 5–10 μm. This dominance arises because in these thin microbeams, the reduced size significantly diminishes the force attributable to pressure, as shown analytically and numerically for a single beam in Miles *et al.* (2019) and experimentally and analytically for spider silk in Zhou and Miles (2017).

To demonstrate that the movable structure shown in Fig. 4 senses air flow, it should be noted that the structure's complexity makes it difficult to derive an analytical solution for the relationship between the displacement of the movable electrode and particle velocity. In addition, conducting acoustic testing in an anechoic chamber with inviscid air is not feasible. Therefore, a finite element analysis (FEA) model, using COMSOL Multiphysics (COMSOL, Inc., Burlington, MA), is employed to examine the effect of viscosity on the acoustic response of the movable structure when a plane wave sound approaches the movable electrode parallel to the device layer. In this simulation, thermoviscous acoustic physics is modeled using an isothermal condition that reflects the ambient environment, coupled to the nonrigid movable structure through a fluid-structure interface (FSI).

Figure 5 shows a two-dimensional (2D) slice of a three-dimensional (3D) simulation of the total acoustic velocity in the *z*-direction inside the cavity and around the movable structure. In these calculations, the bulk viscosity was taken to be 1.10×10^{-5} Pa s, and the dynamic viscosity was taken to be 1.84×10^{-5} Pa s. The FEA results presented in Fig. 6 demonstrate that in the absence of viscosity, the movement of the structure in response to sound is minimal compared to its sound-induced movement when viscosity is present. This suggests that the viscous force caused by the flow is a much more important contributor to the sound-induced movement of the electrode than the sound pressure alone, which is not related to viscosity. A more detailed experimental and computational examination of the viscous flow in the cavity without the sensing structure has shown a similar result as presented in Lai *et al.* (2025). The ratio of V/V_{air} is analyzed, where V denotes the local velocity in the *z*-direction, and V_{air} is the velocity of acoustic particles far from the structure. Blue represents acoustic velocity in the negative *z*-direction, whereas red indicates particles moving out of the cavity. This results in an unbalanced

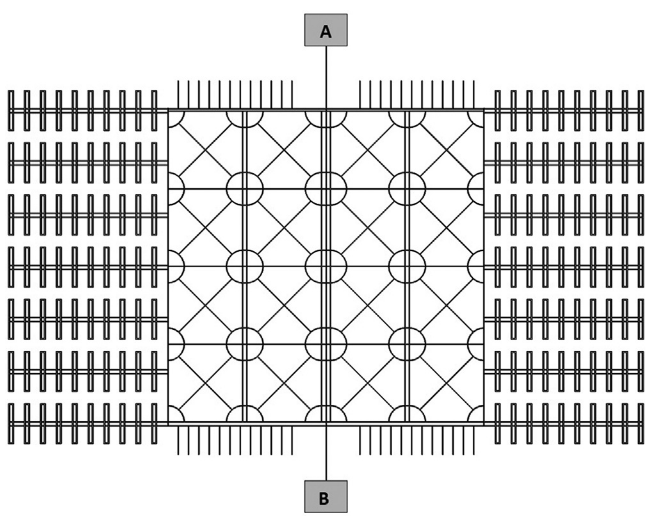

FIG. 4. Plan view of the movable structure, which is a perforated and thin component supported by a flexible hinge fixed at points (A) and (B). Its porous design not only reduces weight but also facilitates airflow through the structure.

https://doi.org/10.1121/10.0036772

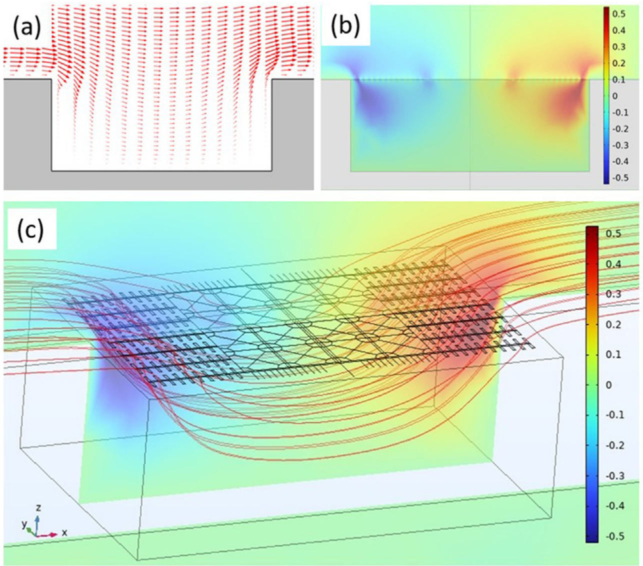

FIG. 5. FEA results showing the acoustic velocity distribution in the cavity at 1000 Hz. (a) A 2D simulation illustrates acoustic particle velocity in the cavity without fins. (b) A 2D cross-sectional view of a 3D model highlighting the interaction between sound and the fins is shown; the ratio V/V_{air} is displayed, where V is the local particle velocity in the z-direction, and V_{air} is the incoming acoustic particle velocity away from the chip. (c) A 3D visualization of the thermoviscous acoustic interaction with the movable electrode shows flow lines around the microbeams.

viscous force that causes vibrational rotation of the movable structure around its hinges.

E. Capacitance estimation

The interdigitated sets of comb fins depicted in Figs. 3 and 4 are designed to maximize the capacitance and proximity of the moving electrode while minimizing the mass of the structure and added viscous damping (creating undesirable viscous shear force between fixed and moving electrodes). The moving structure consists of 14 comb fins, which are all connected through microbeams. Using the boundary element method (BEM), the capacitance between each set is calculated. The predicted total capacitance is shown in Fig. 7. The maximum capacitance of 0.5 pF is achieved when the moving element is resting in its position horizontally. At this angle, the derivative of capacitance with respect to tip displacement is also zero as expected.

The initial deflection of the tip of the moving structure, relative to its undisplaced position, was measured using an optical profilometer. It was found to be approximately 0.2 μm on average. Our boundary element model enabled the prediction of the capacitance as a function of the structure's deflection. The predicted capacitance and its derivative are depicted in Fig. 7. The measured deflection then results in a predicted change in capacitance with deflection of approximately -6×10^{-9} F/m. The gain of the charge amplifier used to convert the capacitance of the sensor to an electronic signal is set using a capacitor, Cf, in the circuit displayed in Fig. 8. The value of Cf was set to be Cf = 1 pF. This capacitance and an initial deflection of 0.2 μm in Eq. (1) leads to an electrical sensitivity, dV/dx (where x represents the deflection of the tip of the moving structure), to be approximately 3.6 V/mm. This predicted sensitivity deviates by only 10% from the measured value of 4 V/mm.

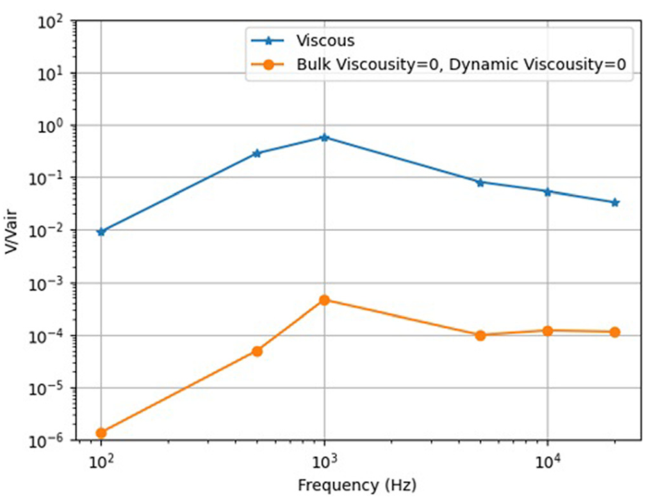

FIG. 6. FEA results comparing the acoustic response relative to air particle velocity for a moving structure above a cavity in a plane wave sound field of 1 Pa. The comparison is between the viscous and inviscid cases, where viscosity is set to zero for the inviscid case. For the viscous case, bulk viscosity is 1.10×10^{-5} Pa s and dynamic viscosity is 1.84×10^{-5} Pa s at 25 °C, as read from COMSOL Multiphysics.

II. THE CIRCUIT

The charge amplifier circuit shown in Fig. 8 has been realized using an operational amplifier for obtaining an electronic output. The circuit consists of surface-mounted electronic components that output the signal from the MEMS chip mounted on the opposite side of the circuit board. The output signals are connected using a micro-High-Definition Multimedia Interface (HDMI) connector as displayed in Figs. 9 and 10.

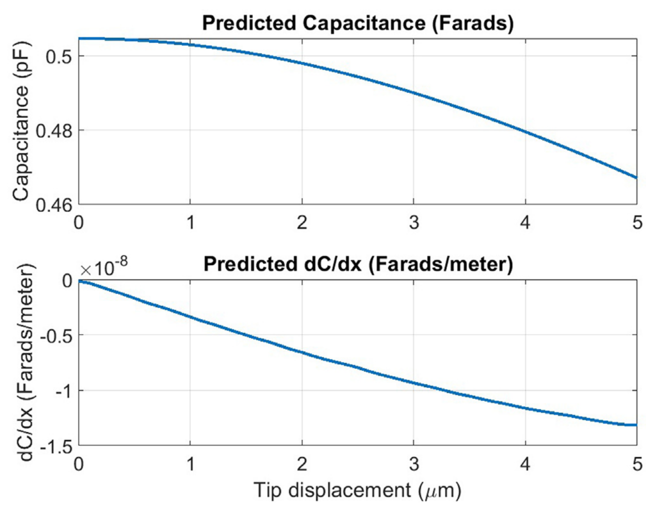

FIG. 7. Predicted capacitance and its derivative with respect to the tip displacement of the moving element. The maximum capacitance is a little above 0.5 pF when there is no initial deflection. The capacitance varies quite linearly for small deflections about the static, equilibrium positions of the moving electrode.

https://doi.org/10.1121/10.0036772

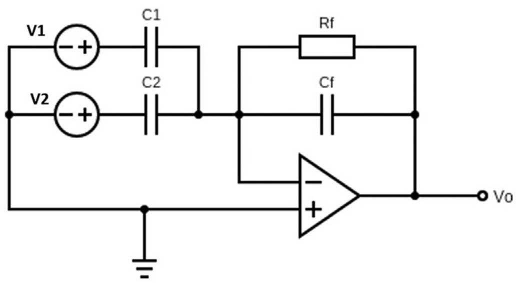

FIG. 8. Operational amplifier circuit with negative feedback serves as a charge amplifier to enable capacitive sensing. $R_f = 10G\Omega,\ C_f = 1\,\text{pF}$.

C_1 and C_2, shown in Fig. 8, represent the capacitors created by the left and right sides of the moving structure with the fixed electrodes. Bias voltages of $\pm 6\,\text{V}$ are applied to each of the fixed electrodes with opposite polarity ($V_1 = -V_2 \approx 6\ \text{V}$), whereas the moving electrode is virtually grounded using a charge amplifier realized using an OPA657 (Texas Instruments, Dallas, TX). A small rotation of the movable electrode around its equilibrium position results in a change in output voltage, V_o.

The change in output voltage resulting from a change in rotation is given by (Miles *et al.*, 2015)

$$\frac{dv_o}{d\theta} = -\frac{\frac{dC_1}{d\theta}V_1 + \frac{dC_2}{d\theta}V_2}{C_f}. \tag{1}$$

If the moving structure is initially displaced by an angle θ_0, the electrical sensitivity $H_{\delta v_o}(\omega)$, caused by a small rotation of δ, is

$$H_{\delta v_o}(\omega) = -\frac{\left.\frac{dC_1}{d\theta}\right|_{\theta_0} V_1 + \left.\frac{dC_2}{d\theta}\right|_{\theta_0} V_2}{C_f}. \tag{2}$$

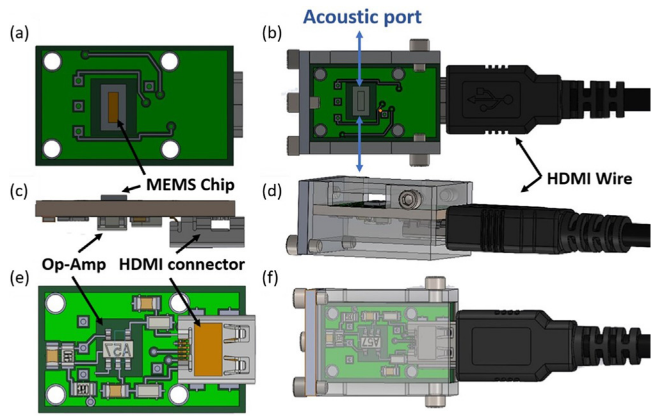

FIG. 9. Readout circuit board is enclosed in an aluminum box as a shield and connected to a micro-HDMI cable. (a) and (b) show the bottom view of the printed circuit board (PCB) [blue arrows in (b) show the acoustic port, which is the most sensitive direction of the flow-sensing MEMS microphone], (c) and (d) depict the side view of the PCB, and (e) and (f) illustrate the top view of the PCB with and without the aluminum box, respectively.

If the transfer function $H_{P\delta}(\omega)$ between the small rotation δ and the amplitude of the plane wave P are known, the output signal from the flow-sensing microphone resulting from an acoustic plane wave with amplitude P can be written as

$$H_{Pv_0}(\omega) = H_{\delta v_0}(\omega) H_{P\delta}(\omega). \tag{3}$$

III. RESULTS

Measured results were obtained using our anechoic chamber at the State University of New York (SUNY) Binghamton. This facility ensured an ideal plane wave sound input at all frequencies above 80 Hz. The experimental setup is shown in Fig. 11(a). The chip and circuit board

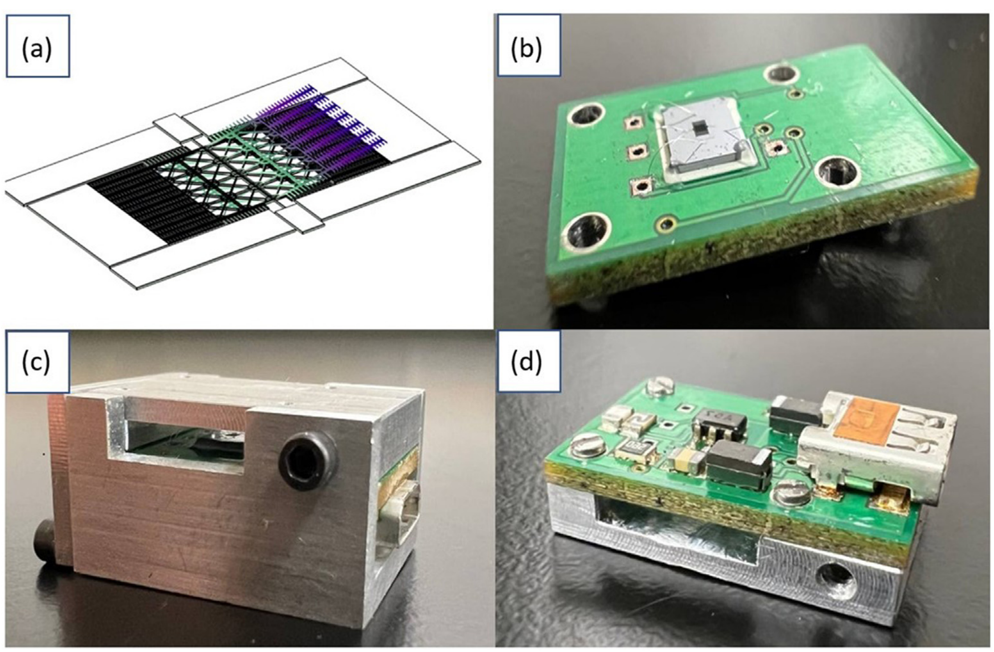

FIG. 10. Schematic of the microphone prototype shows (a) the device layer, (b) the chip on the back side of the circuit board, (c) the circuit board and the chip inside the aluminum box as a Faraday cage, and (d) the electronic side of the circuit board.

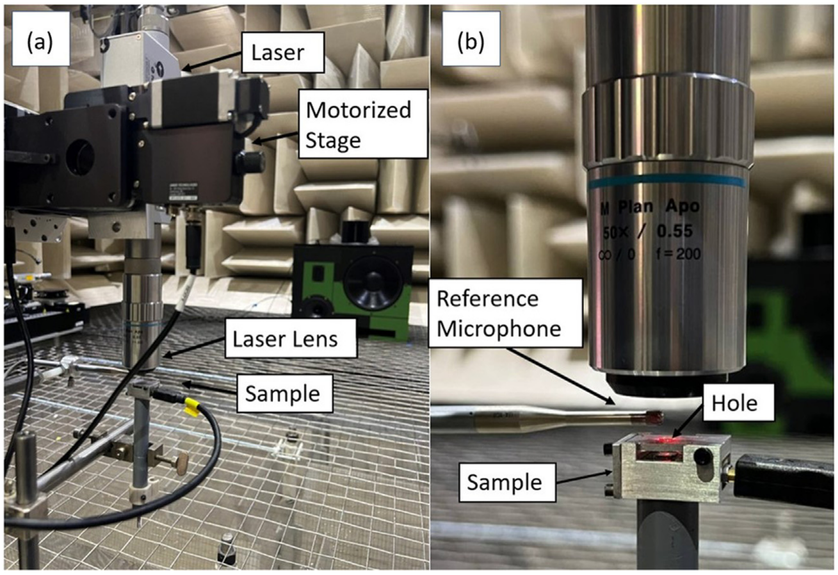

FIG. 11. Testing environment in the anechoic chamber at Binghamton University depicts (a) the setup for measuring the frequency response and sensitivity and (b) a close-up image of the sample setup displaying the position of the hole in the aluminum box that allows the laser to shine on the moving electrode inside the box.

are enclosed inside a small aluminum package, which also serves as a Faraday cage to reduce the electrical noise and allows measuring in the most sensitive direction depicted in Figs. 9 and 10. The sound is generated and played by a loudspeaker that is 3 m away from the testing position. A Polytec laser Doppler vibrometer (Polytec OFV-534, Polytec GmbH, Waldbronn Germany) is focused on the tip of the moving electrode to read its velocity. The voltage output from the operational amplifier and the signal from a Bruel and Kjaer 4138 1/8 in. reference microphone (Darmstadt, Germany) along with the signal from the laser are connected to a National Instruments NI PXI1033 data acquisition system (National Instruments, Austin, TX). Details of the acoustic measurement procedure can be found in Lai *et al.* (2022).

Measurements have indicated that the sound field in the vicinity of the microphone being tested closely approximates that of an ideal plane acoustic wave. Because the field can be approximated by a simple plane wave, the sound pressure and acoustic particle velocity are related by the acoustic impedance, $\rho c \approx 415\,\mathrm{Pa\,s/m}$. This allows us to use the signal from the reference microphone to estimate the acoustic particle velocity sensed by the microphone.

A. Measured microphone output

When the sound is played, the velocity of the air particles exerts a viscous force on the thin beams in the middle, movable electrode. This displacement is measured by the laser vibrometer and plotted with respect to the air particle velocity as calculated by the measured pressure using the Bruel and Kjaer 4138 1/8 in. reference microphone, which is placed close to the prototype in the plane wave acoustic field. The result, depicted in Fig. 12, indicates that the middle electrode moves with a velocity close to that of the air particles. This movement generates an output signal caused by the capacitive sensing mechanism between the moving and fixed electrodes. The voltage output of the microphone

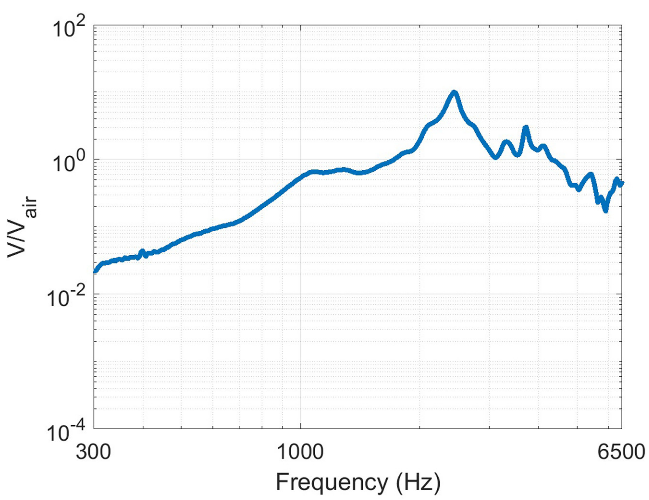

FIG. 12. Measured velocity of the movable electrode tip, V, relative to the air particle velocity, V_{air}, under biased electrode conditions. The results indicate that the tip of the movable electrode closely follows the velocity of the surrounding air particles in a plane sound wave.

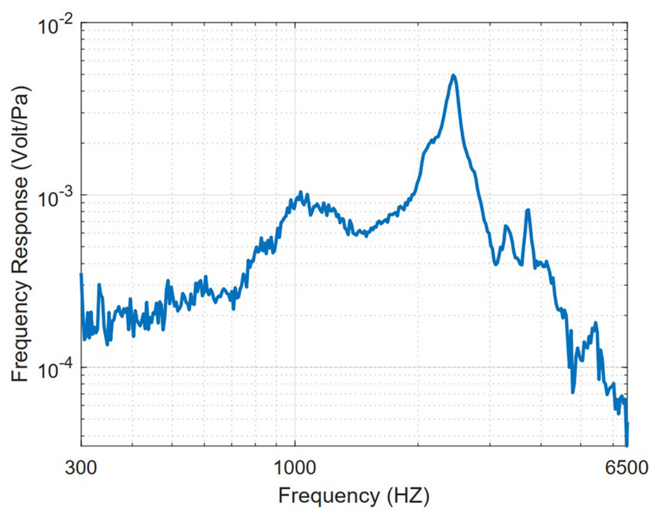

FIG. 13. Measured acoustic sensitivity in volts per pascal with sound incident in the most sensitive direction.

https://doi.org/10.1121/10.0036772

per Pascal as a function of frequency for a plane sound wave is presented in Fig. 13, where the microphone's sensitivity is approximately 1 mV/Pa.

B. Noise floor of the microphone

In the absence of any sound input, the output of the microphone will be the result of a combination of the electrical noise in the circuit and thermal-mechanical noise of the sensing electrode. Thermal-mechanical noise is generated in any microphone because of the momentum transfer to the moving electrode resulting from its interaction with the random motion of surrounding air molecules (Miles, 2020). This thermal-mechanical response of the moving electrode has been measured using the laser vibrometer. The measured square root of the power spectral density of the random thermal-mechanical response is shown in Fig. 14. This thermal-mechanical response is transduced by the readout circuit and will combine with the noise generated within the circuit itself.

The square root of the power spectral density of the output noise voltage is displayed in Fig. 15. Because the frequency dependence of the thermal-mechanical noise depicted in Fig. 14 shows two peaks, one peak at about 2500 Hz and the other peak at about 6 kHz, which do not appear in the measured total output noise of Fig. 15, we can conclude that the total output noise is primarily composed of electronic rather than thermal-mechanical sources. Figure 16 shows the square root of the power spectral density of the sound pressure-referred noise, rtPSD $\left(\mathrm{Pa}/\sqrt{\mathrm{Hz}}\right)$ in the frequency domain for frequencies from 300 to 6500 Hz.

C. Measured microphone directivity

Because this microphone is designed to have a highly porous, low-mass moving structure and, hence, intended to respond to the motion of the air in a sound field rather than

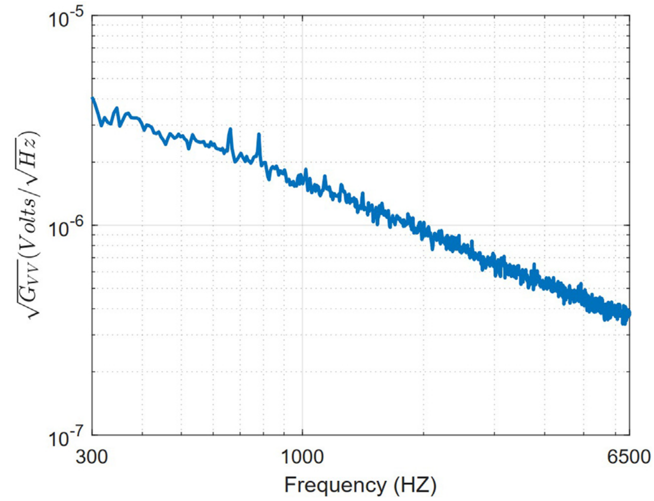

FIG. 15. Circuit output noise measured in $\mathrm{V}/\sqrt{\mathrm{Hz}}$. As no resonance peak is observed in the output noise, it indicates that circuit noise is the predominant source of the output noise.

pressure alone, as in virtually all other microphone designs, the output signal can be expected to depend on the direction of the incident sound wave. This is because velocity is a vector with a magnitude and a direction, whereas pressure is a scalar, acting normal to every surface.

Spatial gradients perpendicular to the axis of rotation will result in unbalanced forces on the air, causing acoustic flow parallel to the plane of the sensing structure. This flow will travel into and out of the cavity behind the sensing structure, producing a viscous-driven moment about the axis of rotation. This flow is examined in more detail in Lai *et al.* (2025).

For measuring the directional response, the flow-sensing microphone is placed on a motorized rotational stage while the position of the loudspeaker is fixed and at a distance of 3 m from the microphone in our anechoic chamber as shown in Fig. 17(d). The output voltage signal is

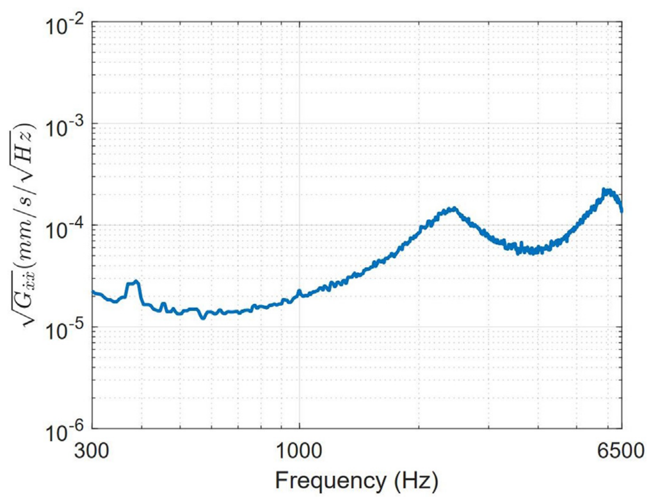

FIG. 14. Measured thermal noise at the tip of the moving electrode measured in $\mathrm{mm/s}/\sqrt{\mathrm{Hz}}$. This graph indicates that thermal noise is influenced by two resonant modes. Design enhancements could mitigate these modes' responses or shift them to less critical frequencies to achieve an even lower noise floor.

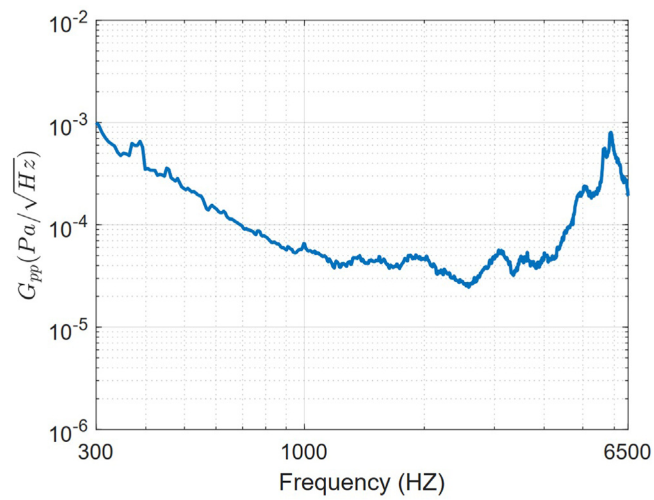

FIG. 16. Input pressure-referred noise is measured in $\mathrm{Pa}/\sqrt{\mathrm{Hz}}$ for a plane acoustic wave, calculated from the acoustic response (V/V_{air}), and the thermal noise response is measured by the laser vibrometer.

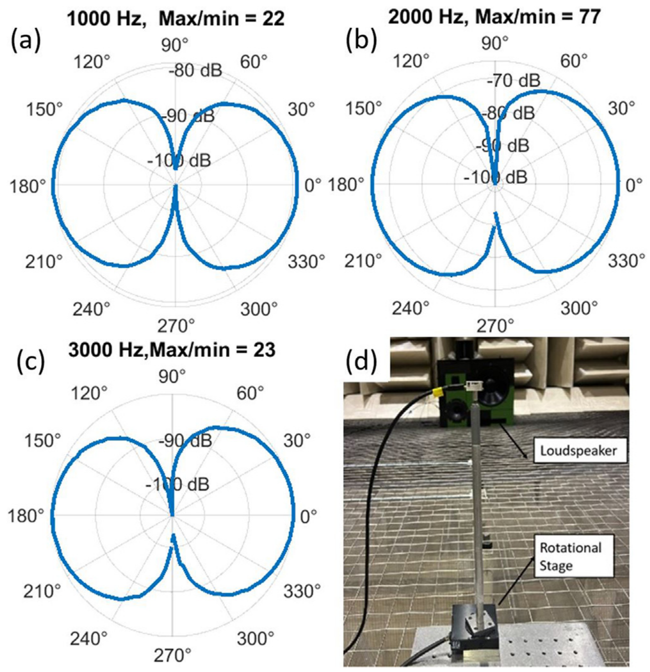

FIG. 17. (a), (b), (c) Measured directivities of the flow-sensing MEMS microphone at 1000, 2000, and 3000 Hz, respectively, in the most sensitive directions are depicted. (d) presents the setup for directivity measurement. The observed directivity patterns closely resemble those of an ideal directional microphone, effectively hearing sound waves from specific directions while efficiently canceling noise or sounds from other directions.

measured as the microphone is rotated from 0 to 360 deg relative to the direction of propagation of the plane acoustic wave. The output is measured for each rotation angle when a pure tone sound is played by the loudspeaker. The output voltage then is curve fitted in the time-domain to determine its amplitude and phase relative to that of the reference microphone for each input frequency (Miles, 2020). It is then normalized by the result obtained for the most sensitive direction of the microphone. Results in Figs. 17(a)–17(c) show that the microphone has a typical figure eight directivity curve, as expected. As a result, it can successfully reject the sound when it is played perpendicular to the most sensitive direction of the microphone with the ratio of maximum to minimum of 22, 77, and 23 for 1000, 2000, and 3000 Hz, respectively, shown in Figs. 17(a)–17(c).

IV. CONCLUSIONS

The flow-sensing MEMS microphone presented here consists of a lightweight, porous, movable structure that is driven by viscous forces between it and the moving air in a sound field. The structure responds to the sound-driven flow into and out of a hole in the silicon chip, which is created by a backside through-wafer etch. The structure is generated using conventional microfabrication methods.

Measured results show that even if the design is not yet completely optimized, it can successfully result in a sensitivity of approximately 5 mV/Pa, whereas the sound pressure-referred noise is between 10^{-4} and 10^{-5} $\mathrm{Pa}/\sqrt{\mathrm{Hz}}$. The directionality of the microphone allows it to attenuate the sound in a perpendicular direction relative to its most sensitive direction with a ratio of the maximum to the minimum output of 77. The maximum capacitance of the microphone is slightly above 0.5 pF, whereas its derivative with respect to displacement will change quite linearly, which is a very desirable feature in microphone design.

Although numerous features of the design have not yet been fully optimized, the results presented here demonstrate that sensing acoustic flow can be a viable alternative to sensing sound pressure alone; sensing flow can be highly advantageous in many acoustic sensing applications.

ACKNOWLEDGMENTS

Research reported in this publication was supported by the National Institute on Deafness and Other Communication Disorders of the National Institutes of Health under Award No. R01DC017720 to R.M. The fabrication of the prototype device was performed, in part, at the Cornell NanoScale Facility, a National Nanotechnology Coordinated Infrastructure (NNCI) member supported by NSF Grant No. NNCI-2025233. Special thanks to Jaron Cui for assistance in the design of the lithographic masks and Maryam Moradian (maryam.moradian@student.uni-siegen.de) for assisting with the drawings.

AUTHOR DECLARATIONS

Conflict of Interest

The authors have no conflicts to disclose.

Author Contributions

Johar Pourghader wrote the initial draft, performed analysis and design of the capacitive sensing, conducted finite element analysis (FEA) for modal, solid structure, and thermo-viscous acoustic simulations, and conducted experimental testing to obtain results for the acoustic and noise response of the chip. Weili Cui carried out the detailed design of the MEMS structure, developed the silicon microfabrication process, and performed all fabrication steps to produce working microphone prototypes. Junpeng Lai developed the process for measuring and characterizing the acoustic performance of the prototype. Mahdi Farahikia developed finite element models for the visco-thermal acoustics of the structure to guide the design process. Changhong Ke participated in the overall design of the research effort and provided advice on fabrication and characterization. Morteza Karimi assisted in characterizing the acoustic response and noise of the silicon chips after fabrication. Ronald Miles edited the manuscript and provided overall direction for the research.

DATA AVAILABILITY

The data that support the findings of this study are available within the article.

Barth, F. G., Wastl, U., Humphrey, J. A. C., and Devarakonda, R. (**1993**). "Dynamics of arthropod filiform hairs. II. Mechanical properties of spider trichobothria (*Cupiennius salei* Keys.),” Philos. Trans. R. Soc. London, Ser. B **340**(1294), 445–461.

Chen, J., Engel, J., Chen, N., Pandya, S., Coombs, S., and Liu, C. (**2006**). “Artificial lateral line and hydrodynamic object tracking,” in *19th IEEE International Conference on Micro Electro Mechanical Systems*, Istanbul, Turkey (January 22-26, 2006) (IEEE, New York), pp. 694–697.

Chen, J., Fan, Z., Zou, J., Engel, J., and Liu, C. (**2003**). “Two-dimensional micromachined flow sensor array for fluid mechanics studies,” J. Aerosp. Eng. **16**(2), 85–97.

Coombs, S. (**2001**). “Smart skins: Information processing by lateral line flow sensors,” Auton. Robots **11**, 255–261.

Dagher, S. (**2020**). “Design of a MEMS microphone based on a new device architecture,” Ph.D. thesis, Le Mans Université, Le Mans, France.

De Bree, H.-E. (**2003**). “The microflown, an acoustic particle velocity sensor,” Acoust. Aust. **31**(3), 91–94, available at https://api.semanticscholar.org/CorpusID:125488053.

Dijkstra, M., Van Baar, J., Wiegerink, R. J., Lammerink, T. S., De Boer, J., and Krijnen, G. J. (**2005**). “Artificial sensory hairs based on the flow sensitive receptor hairs of crickets,” J. Micromech. Microeng. **15**(7), S132–S138.

Fan, Z., Chen, J., Zou, J., Bullen, D., Liu, C., and Delcomyn, F. (**2002**). “Design and fabrication of artificial lateral line flow sensors,” J. Micromech. Microeng. **12**(5), 655–661.

Farkasovská, Z., and Bil’ová, M. (**2012**). “Advanced methods for improving the acoustic quality of the products,” in *International Multidisciplinary Scientific GeoConference: SGEM*, Albania, Bulgaria (June 17-23, 2012) (STEF92 Technology Ltd., Sofia, Bulgaria), Vol. 5, p. 37.

Han, Z., Liu, L., Wang, K., Song, H., Chen, D., Wang, Z., Niu, S., Zhang, J., and Ren, L. (**2018**). “Artificial hair-like sensors inspired from nature: A review,” J. Bionic Eng. **15**, 409–434.

Humphrey, J. A. C., and Barth, F. G. (**2007**). “Medium flow-sensing hairs: Biomechanics and models,” Adv. Insect Physiol. **34**, 1–80.

Humphrey, J. A. C., Devarakonda, R., Iglesias, I., and Barth, F. G. (**1993**). “Dynamics of arthropod filiform hairs. I. Mathematical modelling of the hair and air motions,” Philos. Trans. R. Soc. London, Ser. B **340**(1294), 423–444.

Krijnen, G. J., Dijkstra, M., van Baar, J. J., Shankar, S. S., Kuipers, W. J., de Boer, R. J., Altpeter, D., Lammerink, T. S., and Wiegerink, R. (**2006**). “MEMS based hair flow-sensors as model systems for acoustic perception studies,” Nanotechnology **17**(4), S84–S89.

Lai, J., Farahikia, M., Karimi, M., Liu, Z., Jiang, Y., Ke, C., and Miles, R. (**2024**). “Effect of size on the thermal noise and acoustic response of viscous-driven microbeams,” J. Acoust. Soc. Am. **155**(4), 2561–2576.

Lai, J., Karimi, M., and Miles, R. (**2022**). “Methods for accurate acoustic characterization with ultra-low noise and minimal effect from reflection wave,” J. Acoust. Soc. Am. **152**(4), A194.

Lai, J., Liu, Z., Karimi, M., Farahikia, M., Cui, W., Pourghader, J., Aghazadeh, S., Ke, C., and Miles, R. (**2025**). “A small cavity for detecting sound-induced flow,” J. Acoust. Soc. Am. **157**(1), 29–42.

Landolfa, M., and Jacobs, G. (**1995**). “Direction sensitivity of the filiform hair population of the cricket cereal system,” J. Comp. Physiol. A **177**, 759–766.

McHenry, M. J., Strother, J. A., and Van Netten, S. M. (**2008**). “Mechanical filtering by the boundary layer and fluid–structure interaction in the superficial neuromast of the fish lateral line system,” J. Comp. Physiol. A **194**, 795–810.

McHenry, M. J., and van Netten, S. M. (**2007**). “The flexural stiffness of superficial neuromasts in the zebrafish (*Danio rerio*) lateral line,” J. Exp. Biol. **210**(23), 4244–4253.

Miles, R., Robert, D., and Hoy, R. (**1995**). “Mechanically coupled ears for directional hearing in the parasitoid fly *Ormia ochracea*,” J. Acoust. Soc. Am. **98**(6), 3059–3070.

Miles, R., Su, Q., Cui, W., Shetye, M., Degertekin, F., Bicen, B., Garcia, C., Jones, S., and Hall, N. (**2009**). “A low-noise differential microphone inspired by the ears of the parasitoid fly *Ormia ochracea*,” J. Acoust. Soc. Am. **125**(4), 2013–2026.

Miles, R. N. (**2020**). *Physical Approach to Engineering Acoustics* (Springer, New York).

Miles, R. N., Cui, W., Su, Q. T., and Homentcovschi, D. (**2015**). “A MEMS low-noise sound pressure gradient microphone with capacitive sensing,” J. Microelectromech. Syst. **24**(1), 241–248.

Miles, R. N., Farahikia, M., Leahy, S., and Aziz, A. A. (**2019**). “A flow-sensing velocity microphone,” in *2019 IEEE SENSORS*, Montreal, Canada (October 27-30, 2019) (IEEE, New York), pp. 1–4.

Moshizi, S. A., Azadi, S., Belford, A., Razmjou, A., Wu, S., Han, Z. J., and Asadnia, M. (**2020**). “Development of an ultra-sensitive and flexible piezoresistive flow sensor using vertical graphene nanosheets,” Nano-Micro Lett. **12**, 109.

Ozdogan, M., Towfighian, S., and Miles, R. N. (**2020**). “Modeling and characterization of a pull-in free MEMS microphone,” IEEE Sens. J. **20**(12), 6314–6323.

Pandya, S., Yang, Y., Jones, D. L., Engel, J., and Liu, C. (**2006**). “Multisensor processing algorithms for underwater dipole localization and tracking using MEMS artificial lateral-line sensors,” EURASIP J. Adv. Signal Process. **2006**(1), 076593.

Peng, T.-H., Hsu, H.-J., and Huang, J. H. (**2025**). “Analysis of structural design variations in MEMS capacitive microphones,” Sensors**25**(3), 900.

Shimozawa, T., Kumagai, T., and Baba, Y. (**1998**). “Structural scaling and functional design of the cercal wind-receptor hairs of cricket,” J. Comp. Physiol. A **183**, 171–186.

Tautz, J. (**1979**). “Reception of particle oscillation in a medium—An unorthodox sensory capacity,” Naturwissenschaften **66**(9), 452–461.

Tautz, J., and Markl, H. (**1978**). “Caterpillars detect flying wasps by hairs sensitive to airborne vibration,” Behav. Ecol. Sociobiol. **4**, 101–110.

Van Der Eerden, F., De Bree, H., and Tijdeman, H. (**1998**). “Experiments with a new acoustic particle velocity sensor in an impedance tube,” Sens. Actuators A **69**(2), 126–133.

Weinberger, J., Olson, H. F., and Massa, F. (**1933**). “A uni-directional ribbon microphone,” J. Acoust. Soc. Am. **5**(2), 139–147.

Yang, Y., Chen, J., Engel, J., Pandya, S., Chen, N., Tucker, C., Coombs, S., Jones, D. L., and Liu, C. (**2006**). “Distant touch hydrodynamic imaging with an artificial lateral line,” Proc. Natl. Acad. Sci. U.S.A. **103**(50), 18891–18895.

Yang, Y., Nguyen, N., Chen, N., Lockwood, M., Tucker, C., Hu, H., Bleckmann, H., Liu, C., and Jones, D. L. (**2010**). “Artificial lateral line with biomimetic neuromasts to emulate fish sensing,” Bioinspir. Biomim. **5**(1), 016001.

Zhang, X., Liu, D., Li, X., Liu, Y., Tu, Q., and Zhou, Y. (**2019**). “Particle velocity sensor and its application in near-field noise scanning measurement,” J. Appl. Math. Phys. **7**(11), 2902–2908.

Zhou, J., Lai, J., Menda, G., Stafstrom, J. A., Miles, C. I., Hoy, R. R., and Miles, R. N. (**2022**). “Outsourced hearing in an orb-weaving spider that uses its web as an auditory sensor,” Proc. Natl. Acad. Sci. U.S.A. **119**(14), e2122789119.

Zhou, J., and Miles, R. N. (**2017**). “Sensing fluctuating airflow with spider silk,” Proc. Natl. Acad. Sci. U.S.A. **114**(46), 12120–12125.